




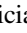
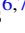






Constraints on the Galactic Inner Halo Assembly History from the Age Gradient of Blue Horizontal-branch Stars

Devin D. Whitten^{1,2} , Timothy C. Beers^{1,2} , Vinicius M. Placco^{1,2} , Rafael M. Santucci^{3,4} , Pavel Denissenkov^{2,5} ,
Patricia B. Tissera^{6,7} , Andrea Mejías^{6,7} , Nina Hernitschek⁸ , and Daniela Carollo⁹ 

¹Department of Physics, University of Notre Dame, Notre Dame, IN 46556, USA

²JINA Center for the Evolution of the Elements, USA

³Instituto de Estudos Sócio-Ambientais, Planetário, Universidade Federal de Goiás, Goiânia, GO 74055-140, Brazil

⁴Instituto de Física, Universidade Federal de Goiás, Campus Samambaia, Goiânia, GO 74001-970, Brazil

⁵Department of Physics & Astronomy, University of Victoria, Victoria, BC, V8W 2Y2, Canada

⁶Departamento de Ciencias Físicas, Universidad Andres Bello, Av. Republica 220, Santiago, Chile

⁷Millennium Institute of Astrophysics, Av. Republica 220, Santiago, Chile

⁸Division of Physics, Mathematics and Astronomy, Caltech, Pasadena, CA 91125, USA

⁹INAF—Astrophysical Observatory of Turin, I-10025 Torino, Italy

Received 2019 May 8; revised 2019 September 5; accepted 2019 September 6; published 2019 October 14

Abstract

We present an analysis of the relative age distribution of the Milky Way halo, based on samples of blue horizontal-branch (BHB) stars obtained from the Panoramic Survey Telescope and Rapid Response System and *Galaxy Evolution Explorer* photometry, as well a Sloan Digital Sky Survey spectroscopic sample. A machine-learning approach to the selection of BHB stars is developed, using support vector classification, with which we produce chronographic age maps of the Milky Way halo out to 40 kpc from the Galactic center. We identify a characteristic break in the relative age profiles of our BHB samples, corresponding to a Galactocentric radius of $R_{GC} \sim 14$ kpc. Within the break radius, we find an age gradient of -63.4 ± 8.2 Myr kpc^{-1} , which is significantly steeper than obtained by previous studies that did not discern between the inner- and outer-halo regions. The gradient in the relative age profile and the break radius signatures persist after correcting for the influence of metallicity on our spectroscopic calibration sample. We conclude that neither are due to the previously recognized metallicity gradient in the halo, as one passes from the inner-halo to the outer-halo region. Our results are consistent with a dissipational formation of the inner-halo population, involving a few relatively massive progenitor satellites, such as those proposed to account for the assembly of *Gaia*-Enceladus, which then merged with the inner halo of the Milky Way.

Key words: Galaxy: evolution – Galaxy: formation – methods: statistical – stars: horizontal-branch

1. Introduction

The Λ cold dark matter cosmological paradigm describes the hierarchical growth of structure in the universe, where galaxies assemble via mergers of smaller, low-mass systems (White & Rees 1978). The continued process of hierarchical structure formation has largely been confirmed with the discovery of streams, tidal tails, over-densities, and numerous satellite galaxies of the Milky Way (Majewski et al. 2003; Belokurov et al. 2006; Helmi 2008; Martin et al. 2014; Shipp et al. 2018). However, a quantitative description of the assembly history of the Milky Way has eluded consensus.

The structural components of the Milky Way largely retain the signatures of their formation (Freeman & Bland-Hawthorn 2002), and thus present an opportunity to study the process of galaxy formation. The Milky Way halo is of particular importance, as the long dynamical times associated with this low-density component enable the persistence of substructures seen in various stages of their diffusion into the Galaxy. Low-mass stars in the halo can be nearly as old as the universe, while their spatial, kinematic, age, and chemical abundance distributions reflect their origins, whether that be in situ,¹⁰ or in satellite galaxies accreted onto the primordial Milky Way.

Kinematical and chemodynamical studies of the halo have revealed it to comprise at least a dual system (e.g., Gratton et al. 2003; Carollo et al. 2007, 2010; Miceli et al. 2008; Nissen & Schuster 2010; Beers et al. 2012), including a zero to mildly prograde net rotation inner halo with a peak metallicity of $[\text{Fe}/\text{H}] = -1.6$, and net retrograde outer halo with peak $[\text{Fe}/\text{H}] = -2.2$. Galaxy formation simulations predict stellar haloes to be formed mainly by the accretion of satellite galaxies, with contributions from in situ stars (Zolotov et al. 2009; Font et al. 2011; Tissera et al. 2012). The properties of these accreted satellites would imprint features in the chemical abundances, age, and kinematics of the stellar populations in the stellar haloes (Tissera et al. 2013, 2014; Carollo et al. 2018; Fattahi et al. 2019; Fernández-Alvar et al. 2019). These features could be used to constrain the formation histories of the inner and outer regions of the stellar haloes.

Following the second data release from *Gaia* (Gaia Collaboration et al. 2018), Belokurov et al. (2018) demonstrated that halo stars of metallicity $[\text{Fe}/\text{H}] > -1.7$ exhibit highly radial orbits (consistent with the claims of previous authors, e.g., Chiba & Beers 2000), suggesting a major accretion event by a massive ($10^{10} M_{\odot}$) satellite, between 8 and 11 Gyr ago. This progenitor, called the *Gaia* Sausage (Myeong et al. 2018), was confirmed by Helmi et al. (2018), whose findings suggested that the inner halo consists largely of debris from the accretion of a single progenitor, dubbed *Gaia*-Enceladus, provided that *Gaia*-Enceladus encompasses both

¹⁰ In situ stars are taken to be those formed within the virial radius of the progenitor halo, either as a result of dynamical heating of an existing disk component or the transformation of gas brought in by satellite galaxies into stars.

the high eccentricity population from Belokurov et al. (2018) and a retrograde component (Koppelman et al. 2018). Using a sample of ~ 3000 blue horizontal-branch (BHB) stars from the Sloan Digital Sky Survey (SDSS), Lancaster et al. (2019) determined that this ancient structure constitutes at least $\sim 50\%$ of the metal-poor stellar halo within 30 kpc, but acknowledged that it is unclear whether this structure is the residue of a single, two, or more radial infalls, as suggested by recent cosmological studies (Kruijssen et al. 2019). Myeong et al. (2019) provided the dynamical and chemical evidence of an additional accretion episode, distinct from *Gaia*-Enceladus. This satellite, referred to as the Sequoia galaxy (Barbá et al. 2019), contributed a stellar mass of $\sim 5 \times 10^7 M_\odot$ to the Milky Way, comparable to the Fornax dwarf spheroidal. The apparent complexity of the Milky Way assembly history leaves open the possibility that signatures of additional dwarf galaxy mergers may yet persist in the kinematics, chemical, or age distributions of the Milky Way’s oldest stars.

While challenging to estimate, stellar ages are a powerful tool with which to constrain the merger history of the Galaxy. BHB stars have been successfully used to demonstrate a radial age gradient in the halo (Preston et al. 1991; Santucci et al. 2015a; Carollo et al. 2016; Das et al. 2016). Using *UBV* photometry for 4408 candidate field horizontal-branch stars, Preston et al. (1991) demonstrated an increase in the $(B - V)_0$ color of ~ 0.025 mag with Galactocentric distance over $R_G = [2, 12]$ kpc, suggesting a decrease in the mean age of field horizontal-branch stars by a few Gyr. Following a rigorous identification of BHB stars from SDSS/Sloan Extension for Galactic Understanding and Exploration (SEGUE) spectroscopy in Santucci et al. (2015a, 2015b) used de-reddened $(g-r)_0$ photometry of BHB stars to identify an increase in the mean colors of BHB stars from regions close to the Galactic center to ~ 40 kpc, corresponding to an age difference of 2–2.5 Gyr, and produced an age map of the halo system up to ~ 25 kpc. In a later investigation, Carollo et al. (2016) produced age maps up to ~ 60 kpc by employing a large number of BHB stars selected on the basis of their colors from SDSS DR8 (Aihara et al. 2011a). Both works confirm the Preston et al. (1991) result, and reveal the presence of numerous younger substructures in the outer-halo region. Carollo et al. (2016) found a global age gradient of -25.1 ± 1.0 Myr kpc^{-1} , consistent with the result of -30 Myr kpc^{-1} by Das et al. (2016).

In a follow-up study of age gradients for Milky Way-mass galaxies simulated by the Aquarius Project, Carollo et al. (2018) found an overall age gradient in the range of $[-8, -32]$ Myr kpc^{-1} , for which the accreted component of the stellar population is largely responsible. These results suggest that the Milky Way formation history is dominated by the accretion of satellite galaxies with dynamical masses less than $\sim 10^{9.5} M_\odot$.

Using a suite of *N*-body simulations, Amorisco (2017) found that satellites that are accreted at higher redshift, and thus likely possess characteristically older stellar populations, deposit their material farther inside their host galaxies. Age gradients are thus a powerful diagnostic with which to probe the assembly history of the Milky Way. Unfortunately, the pioneering observational investigations were limited by sky coverage, sample size, and selection purity; more detailed studies of the nature of the observed gradient are required to distinguish between the widely varying age profiles seen in simulations of Milky Way-mass galaxies.

Age gradients may also prove complementary to studies of the stellar density profile of the Milky Way, which was demonstrated by Pillepich et al. (2014) to be a powerful diagnostic of a galaxy’s accretion history, in addition to its total stellar mass. In contrast to the density profile of the dark matter halo, the stellar density profile is thought to follow an axisymmetric power law, with a distinct flattening in the inner-halo region, and a characteristic break radius occurring at $r \sim 25$ kpc (e.g., Saha 1985; Sesar et al. 2011; Xue et al. 2015; Hernitschek et al. 2018). The existence of a break radius in a halo’s stellar density profile suggests the possibility of a similar break in its age profile.

In this work, we provide the first evidence for a characteristic break in the relative age profile of the Milky Way stellar halo, using a sample of BHB stars obtained from the Panoramic Rapid Response Survey Telescope (Pan-STARRS1) and the *Galaxy Evolution Explorer* (GALEX). In Section 2, we discuss the various surveys used in the selection of BHB stars. In Section 3, we describe our selection strategy for BHB stars, based on a machine-learning photometric selection methodology. We describe the determination of relative ages for our BHB samples in Section 4, and model the chronographic distribution of these stars using maximum likelihood estimation (MLE). The results of our analysis of the radial age profile of the BHB samples are provided in Section 5. We discuss our interpretation of these results in Section 6, followed by concluding remarks in Section 7.

2. Survey Samples

In this section, we describe the photometric and spectroscopic survey catalogs used in the selection of halo BHB candidates in this work.

2.1. SDSS

We develop our selection methodology using the sample of spectroscopically verified BHB and blue straggler stars (BSSs) from SDSS/SEGUE described in Santucci et al. (2015a), hereby referred to as the SDSS spectroscopic sample. The sample consists of 4772 BHB and 7938 BSSs with medium-resolution ($R \sim 2000$) spectroscopy from SDSS DR8 (Aihara et al. 2011b), to a faint limit of $g \sim 21$. The spectroscopic criteria for the identification of BHB stars in this catalog utilized a number of properties in the stellar spectrum, including Balmer line widths and other gravity-sensitive features. We refer the interested reader to Santucci et al. (2015a) for further details. A similar spectroscopic catalog was developed by Xue et al. (2008), however the Santucci et al. (2015a) sample employed a somewhat larger ($u-g$) selection window, and contains a larger number of BHB stars. The *ugriz* photometry was updated to the most recent version, SDSS DR12 (Abolfathi et al. 2018).

2.2. Pan-STARRS DR1

The Pan-STARRS1 (PS1) survey is a set of high-cadence, multicolor, multi-epoch observations covering a large area of sky (Tonry et al. 2012). The Pan-STARRS1 system is located on the island of Maui, Hawaii, and utilizes a 1.8 m, $f/4.4$ telescope with a 1.4 Gpix detector having a 3.3 deg^2 field-of-view. The stacked PS1 3π Steradian Survey (Chambers et al. 2016) observed the entire sky north of $\delta \sim -30^\circ$, in five bands (g_{P1} , r_{P1} , i_{P1} , z_{P1} , and y_{P1}) to limiting magnitudes of 23.3, 23.2,

23.1, 22.3, and 21.4, respectively. The `StackObjectThin` catalog was queried for objects with $-0.5 < (g - r)_{\text{PS1}} < 0.2$, and `primaryDetection` = 1. A crude star-galaxy rejection, $i\text{PSFMag} - i\text{KronMag} \leq 0.06$ mag, was employed to select for point-source objects (Farrow et al. 2014). As recommended by Flewelling et al. (2016), `GaiaFrameCoordinates` were used for determination of positions, to ensure the highest quality astrometry possible.

2.3. GALEX GUVCat

The *GALEX* (Martin et al. 2005) was the first far- and near-UV survey of the entire sky. The *GALEX* instrument hosted a 50 cm primary mirror, with a beam splitter for simultaneous broadband photometric measurements, in the far-UV ($\lambda_{\text{eff}} \sim 1528 \text{ \AA}$, 1344–1786 \AA) and near-UV ($\lambda_{\text{eff}} \sim 2310 \text{ \AA}$, hereafter NUV). We made use of the *GALEX* All-Sky Imaging survey, in particular the science-enhanced catalogs from GUVcat (Bianchi et al. 2017). This catalog provides a number of improvements to previous releases, including a 10% larger sky coverage and removal of duplicate detections. We cross-matched the *GALEX* GUVCat with Pan-STARRS DR1, hereafter referred to as PS1xGALEX, with a search radius of 3 arcsec, resulting in 1,098,309 unique sources.

2.4. Color Transformations

All catalogs were corrected for Galactic reddening and extinction according to Schlafly & Finkbeiner (2011), where the $E(B - V)$ values included the 14% recalibration of Schlafly et al. (1998), such that $E(B - V) = 0.86 \cdot E(B - V)_{1998}$. Cuts in the point-spread function magnitude errors and the estimated extinction were then made, according to $\text{PSFerr} < 0.2$ mag, and $E(B - V) < 0.1$ mag.

All photometric catalogs in this work were transformed to the corresponding SDSS photometry. For the PS1 catalog, this was done using the calibrations provided in Tonry et al. (2012). For the PS1xGALEX catalog, we developed the following transformation, u_{rlm} , to approximate $u\text{SDSS}$ based on the NUV and g_{PS1} magnitudes and $(g - r)_{\text{PS1}}$ and $(g - i)_{\text{PS1}}$ colors, which resulted in the lowest scatter when compared to alternative color combinations

$$u_{\text{SDSS}} = x_1 \cdot \text{NUV} + x_2 \cdot g_{\text{PS1}} + x_3 \cdot (g - r)_{\text{PS1}} + x_4 \cdot (g - i)_{\text{PS1}}. \quad (1)$$

The resulting calibration is shown in Figure 1 for the subset of the SDSS spectroscopic sample with SDSS, Pan-STARRS, and *GALEX* NUV photometry. The optimal set of coefficients were found to be: $X_1 = 0.22$, $X_2 = 0.78$, $X_3 = -0.21$, $X_4 = -0.14$. Scatter in the calibration is estimated with the median absolute deviation, scaled to the corresponding standard deviation, S_{MAD} , for which we, obtain $S_{\text{MAD}}(u_{\text{SDSS}}) < 0.06$ mag.

3. BHB Candidate Selection

Two unique photometric selections of BHB stars are performed in this work. Although we employ the $(i - z)$ selection developed in Vickers et al. (2012) as a verification of our selection methodology, we demonstrate below that we can obtain a higher sample purity with our new selection method, which we develop with the SDSS spectroscopic sample of Santucci et al. (2015a), described previously.

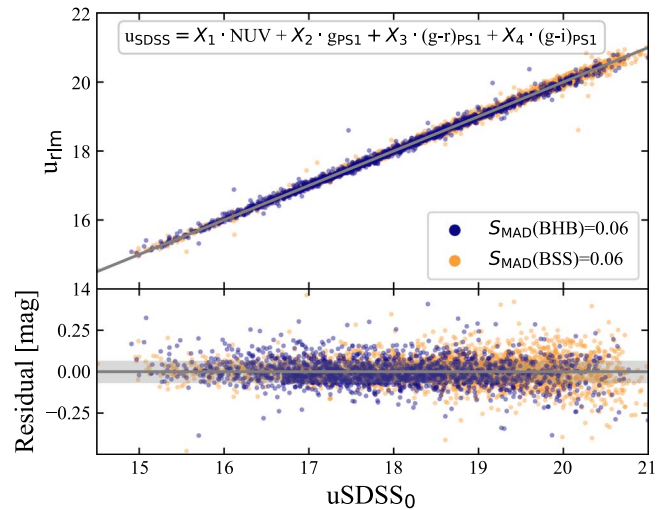


Figure 1. Upper panel: fit of the *GALEX* NUV and SDSS magnitudes and PS1 colors for calibration to u_{SDSS} , according to the model $u_{\text{SDSS}} = x_1 \cdot \text{NUV} + x_2 \cdot g_{\text{PS1}} + x_3 \cdot (g - r)_{\text{PS1}} + x_4 \cdot (g - i)_{\text{PS1}}$. Blue and orange dots indicate spectroscopically confirmed BHB and BSSs, respectively. Lower panel: residual plot of the resulting calibration.

3.1. Support Vector Classification

Two gravity-sensitive colors were used for selection of BHB stars, in order to distinguish between the otherwise higher surface-gravity foreground A-type contaminants—referred to as BSSs in this work—in the initial $(g - r)_0$ selection window. The region of the Balmer break has most often been exploited (Yanny et al. 2000; Sirko et al. 2004; Carollo et al. 2016; Thomas et al. 2018), where a broadening of the Balmer lines is seen for high-gravity stars due to Stark pressure broadening. Additionally, Vickers et al. (2012, 2014) demonstrated the effectiveness of the Paschen break (8200 \AA) as a surface gravity-dependent feature detectable with photometry, although perhaps to a lesser degree than the Balmer break.

We first perform principal component analysis (PCA; Jolliffe 2002) with the inputs $(u - g)_0$, $(g - r)_0$, and $(i - z)_0$ of the SDSS spectroscopic sample. The first and second principal component captured 45% and 41% of the variance, respectively, while the third component captured 14%. We therefore retain all three principal components throughout the selection procedure, described in the following section. An equivalent transformation is performed on all photometric catalogs, using the principal components of the SDSS spectroscopic sample.

We develop the 3D BHB selection function using support vector classification (SVC; Pedregosa et al. 2011). This supervised learning model is a binary classifier which, given data of distinct classes, seeks to find a transformation such that the data classes become maximally separable by a hyperplane in a corresponding feature space. This feature space is dictated by the selected kernel function, the weights of which are optimized during the training procedure. Training of an SVC is therefore concerned with the determination of the appropriate transformation to be applied to the data inputs, such that this separation is effective. To accomplish this, our SVC employs a Gaussian radial basis function (RBF) as a kernel, with which the photometric inputs are transformed. Like many machine-learning algorithms, an SVC with an RBF kernel makes use of two hyperparameters, which must be tuned, in addition to the supervised training process. The first hyperparameter, known

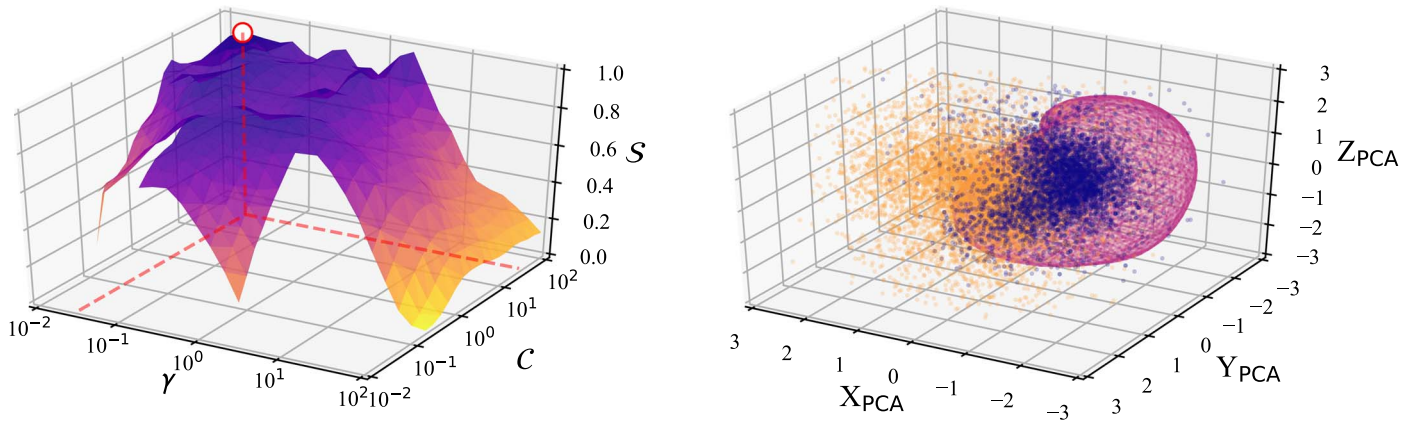


Figure 2. Left panel: hyperparameter optimization for the support vector classifier. Optimal parameters $(C, \gamma) = (31.62, 0.316)$ were chosen where the score, \mathcal{S} , is maximized. Right panel: BHB selection function corresponding to the optimized SVC, in the 3D photometric PCA space. Blue and orange dots denote spectroscopically confirmed BHB stars and BSSs, respectively.

as the regularization parameter, C , governs the extent to which misclassifications are penalized during training. The second hyperparameter is the width of the Gaussian RBF, γ , which controls the extent of data far from the classification boundary. We optimize over the hyperparameters, C and γ , using the SDSS spectroscopic sample, which we split into training and validation sets of 65% and 35%, respectively. The validation fraction of 35% is somewhat higher than typically advised. This fraction was chosen to ensure that the validation sample was sufficiently large to study the affect of the apparent magnitude on the classification purity and recovery fractions.

We compose a grid of SVCs across the hyperparameter range $10^{-2} < C < 10^2$ and $10^{-2} < \gamma < 10^2$, and track the performance of each SVC in terms of the resulting BHB classification purity, f_C , and recovery fraction, f_R . SVC over-training can result in an over-specified decision function and isolated “decision pockets” around individual data in the training set. To check for this, we additionally track the inverse variances of f_C and f_R , which are determined using 30 randomly selected subsamples of the validation set from the SDSS spectroscopic sample. Each subset results in differing classification and recovery fractions, as stars fall into the decision pockets, evidenced by an increase in the classification and recovery variances. We therefore introduce a score parameter for the hyperparameter optimization, \mathcal{S} , which incorporates the classification and recovery fractions, as well as the scale estimates of these values, as determined from the 30 iterative resamples of the data:

$$\mathcal{S}(\gamma, C) = \frac{f_C(\gamma, C) \cdot f_R(\gamma, C)}{S_{\text{MAD}}(f_C(\gamma, C)) \cdot S_{\text{MAD}}(f_R(\gamma, C))}. \quad (2)$$

Here, S_{MAD} denotes the estimate of scale, the median absolute deviation. The result of the grid optimization is shown in the left panel Figure 2, where we take the combination of (C, γ) , which maximize Equation (2). These were found to be $(C, \gamma) = (31.62, 0.316)$, for which the resulting SVC decision boundary is shown in the right panel of Figure 2.

The resulting decision function of the SVC provides the distance, \mathcal{D} , of each star from the hyperplane. While this value is not strictly a probability, the sign and magnitude of \mathcal{D} can be interpreted as a measure of confidence in the resulting classification. We explore the influence of the hyperplane distance on the resulting purity and completeness of the SVC in

the left panel of Figure 3. A marginal increase in the purity is seen with a higher restriction on the hyperplane distance, \mathcal{D} , while the completeness of the selection decreases precipitously. We therefore define our selection function for BHB stars in the PS1xGALEX catalog as the SVC decision boundary at $\mathcal{D} = 0$. Additionally, we investigate in Figure 3 the purity and completeness of our selection function with apparent magnitude. To maintain a purity of $f_C > 80\%$ we implement a magnitude limit of $g_{\text{SDSS},0} < 18.1$ throughout the rest of our work. Finally, we subject the PS1xGALEX catalog to the SVC selection procedure, which resulted in 14,647 BHB candidates. Hereafter, we refer to this selection as the PS1xGALEX-SVC sample.

3.2. The Vickers et al. (2012) Selection

As a validation of the SVC selection methodology, we additionally perform the BHB selection procedure outlined by Vickers et al. (2012) with the PS1 catalog. This method relies on the surface-gravity sensitivity of the Paschen region of the spectral energy distribution, corresponding to the z -band. This selection is defined as follows:

$$-0.3 < (g - r)_0 < 0.0 \quad (3)$$

$$0.5[(g - r)_0 + 0.3] - 0.20 < (i - z)_0 < -0.03. \quad (4)$$

The purity of classification was determined by Vickers et al. (2012) to be $\sim 74\%$, in part because of the limited sensitivity with which this feature can be used to distinguish between the more numerous foreground A-type stars. This selection hereby referred to as the PS1- $(i - z)$ sample, resulted in 20,351 stars.

3.3. Quasar Contamination

Within the faint limit of our samples, $g < 18.1$, we expect a quasar density of $n(g < 18.1) \sim 0.1 \text{ deg}^{-2} \text{ mag}^{-1}$ (Pei 1995), corresponding to a total of $N \sim 10^3$, when taking into account the footprint of Pan-STARRS DR1. Considering the stringent color selections of BHBs from our catalogs, this number is effectively an upper limit, as we expect far less contamination in our SVC selections. We test this expectation by matching the PS1 and PS1xGALEX BHB catalogs with the Large Quasar Astrometric Catalogue (Gattano et al. 2018), a catalog consisting of nearly all known quasars (443,725 sources), including new identifications from the DR12Q release of SDSS and *GAIA* DR1. With a 5 arcsec search radius, we find 22

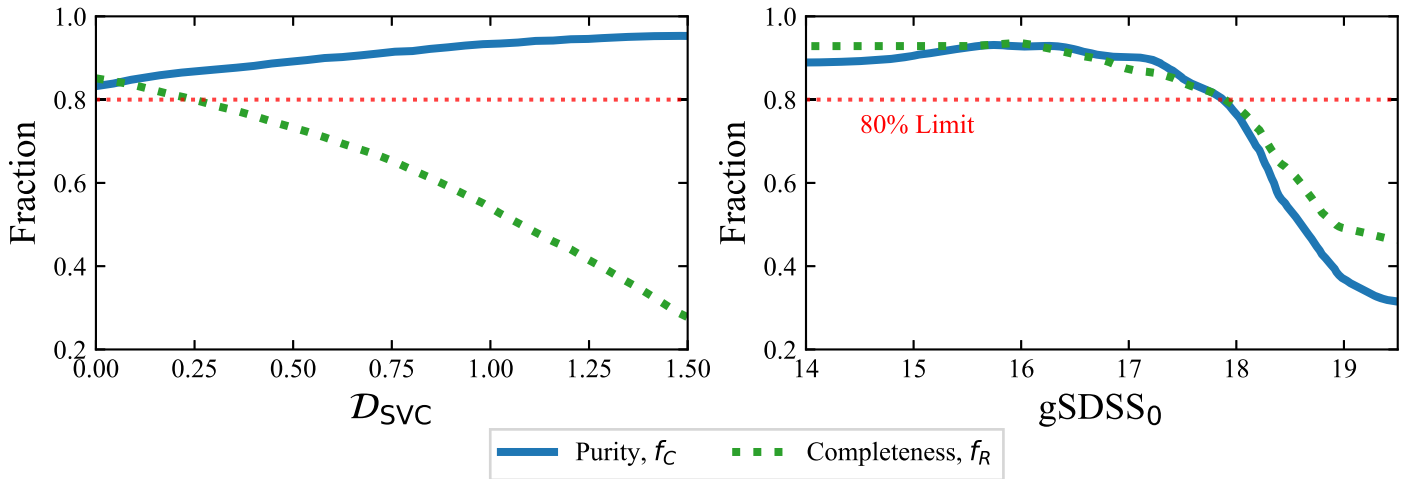


Figure 3. Left panel: BHB purity and completeness of the SVC selection as a function of hyperplane distance, \mathcal{D} . Right panel: purity and sample completeness as a function of apparent magnitude.

unique matches for the PS1xGALEX-SVC sample, and 3380 for the PS1- $(i-z)$ sample. These sources were excluded from our analysis.

3.4. Disk Contamination

Using stellar density models for the thick disk and halo from Mateu & Vivas (2018), we estimate the ratio of thick disk to halo stars at $|Z_G| = 2.5$ kpc to be $\sim 11\%$. This is certainly an overestimation for BHB stars. For a disk star to pass our preliminary $g-r$ selection of $-0.5 < g-r < 0.2$, it would necessarily be hot, $T_{\text{eff}} = 7500\text{--}9500$ K. Stars in this effective temperature range consist of high-surface gravity dwarfs and horizontal-branch stars. These high-surface gravity A-type stars are precisely the type that the photometric selection was designed to remove, on the basis of surface gravity indicators. They differ by at least an order of magnitude in surface gravity from horizontal-branch stars. While it is feasible that horizontal-branch stars do exist in the thick disk, as seen in Bensby et al. (2013), the bulk of giant stars in the thick disk possess significantly higher metallicities than what is thought to be able to produce a BHB star. For the metallicity ranges of the thin and thick disk, these would be red giant clump stars instead, and therefore would not pass our $g-r$ color selection.

4. Methodology

In this section, we discuss the determination of astrometry and photometric age estimates for the BHB samples.

4.1. Astrometry

Distances for stars in the BHB samples are derived from the line-of-sight distance modulus, using the absolute magnitude calibration developed by Deason et al. (2011). We calculate M_g as

$$M_g = 0.434 - 0.169 \cdot (g-r)_0 + 2.319 \cdot (g-r)_0^2 + 20.449 \cdot (g-r)_0^3 + 94.517 \cdot (g-r)_0^4. \quad (5)$$

Scatter in the absolute magnitude calibration was determined to be less than 0.1 mag, corresponding to a distance uncertainty of $\sim 5 - 10\%$. However, the absolute magnitude for BSSs is ~ 2 mag fainter, thus the uncertainty in our distance estimate is

primarily determined by our sample purity. For our SVC sample purity of 80%, the uncertainty in the distance estimates is then $\sim 20\%$.

Together with the equatorial coordinates, (α, δ) , we compute the Galactocentric Cartesian coordinates, X_G, Y_G, Z_G , and Galactic latitude, l_G and b_G , assuming a distance of 8.5 kpc of the Sun from the Galactic center. We then compute the Galactocentric distance, R_G , defined as $R_G = \sqrt{X_G^2 + Y_G^2 + Z_G^2}$. For all samples, we employ a cut of $|Z_G| > 2.5$ kpc and $|b_G| > 15^\circ$, to reduce contamination from disk-system stars, with an additional minimum Galactocentric radius of $R_G > 5$ kpc.

4.2. Chronography

Age estimates for stars in the BHB samples considered in this work are made using the horizontal-branch population synthesis tool of Denissenkov et al. (2017), to which we refer the interested reader for details. Models were generated using revision 7624 of the MESA stellar evolution code (Paxton et al. 2011, 2013), in which solar chemical abundances from Asplund et al. (2009) were adopted. A model grid was constructed, taking into account age, mean $(g-r)_0$ color, and metallicity, which can then be interpolated to estimate an age given $(g-r)_0$ and $[\text{Fe}/\text{H}]$. For the SDSS spectroscopic sample, we use the estimates of $[\text{Fe}/\text{H}]$ produced by the SEGUE Stellar Parameter Pipeline (SSPP; Allende Prieto et al. 2008; Lee et al. 2008a, 2008b). For all other catalogs, we adopt the SDSS sample median $[\text{Fe}/\text{H}] = -1.75$.

4.3. The Dependence of BHB Age Estimates on $[\text{Fe}/\text{H}]$

We first investigate the influence of individual $[\text{Fe}/\text{H}]$ estimates on the inferred age of our BHB stars. To do so, two distinct estimates of age are made for the SDSS spectroscopic sample, first using the individual $[\text{Fe}/\text{H}]$ estimates from the SSPP (hereby referred to as the corrected age estimate, $A_{[\text{Fe}/\text{H}]}$), and second by adopting the median $[\text{Fe}/\text{H}] = -1.75$ for all stars in our sample (hereafter referred to as the photometric age estimate, $A_{(g-r)_0}$).

We use locally weighted scatterplot smoothing (LOWESS; Cleveland 1979) for all profiles visualized in this work, for which we set the local sampling fraction to 25% throughout. Panel (a) of Figure 4 shows the cumulative radial distribution

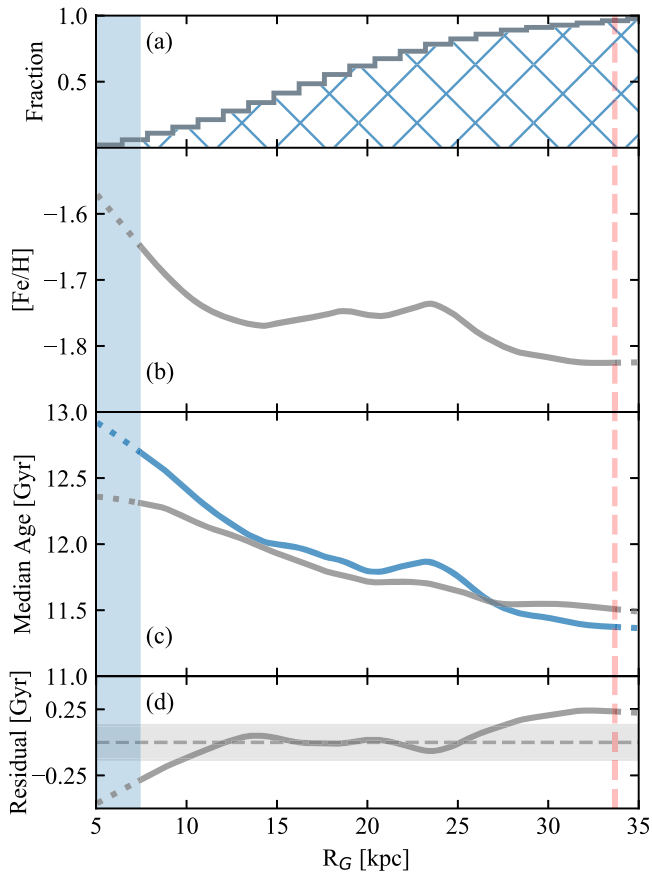


Figure 4. Panel (a): cumulative distribution of BHB stars from the SDSS spectroscopic sample with respect to Galactocentric distance. Panel (b): median metallicity of the SDSS spectroscopic sample with respect to Galactocentric distance. Panel (c): age distributions of the SDSS spectroscopic sample from Santucci et al. (2015a), for both photometric (gray) and corrected age estimates from Denissenkov et al. (2017) (blue). Panel (d): difference between the photometric and corrected age profiles. The broken red line represents the radius beyond which the number of stars decreases below 5%.

of the SDSS spectroscopic sample, and panel (b) shows the median metallicity profile of the sample. In panel (c) of Figure 4, we compare the age estimate obtained from the $(g-r)_0$ photometry to the age estimate corrected for metallicity. A slight offset, of order $A_{(g-r)_0} - A_{[\text{Fe}/\text{H}]} = -100$ Myr, is seen between the profiles. We subtract this offset and plot the resulting residual profile in panel (d). As we are not primarily interested in the absolute ages, we correct for this offset in the photometric age estimate, and find a standard deviation in the residuals of $\sigma = 130$ Myr. Within the Galactocentric radius range of $10 < R_G < 27$ kpc, the LOWESS regression of the corrected residual is within 1σ . We can then assume that, within this range, the photometric age estimate is representative, and we apply the photometric age estimates assuming a median $[\text{Fe}/\text{H}] = -1.75$ for all of the photometric-only BHB catalogs in this work. For further comparison, projected X_G versus Z_G age distributions for both age estimate techniques are provided in Figure 10 of the Appendix.

4.4. Radial Age Profiles

The cumulative radial distribution for each BHB sample is shown in the top panel of Figure 5, followed by the median $(g-r)_0$ and age profiles in the center and bottom panels,

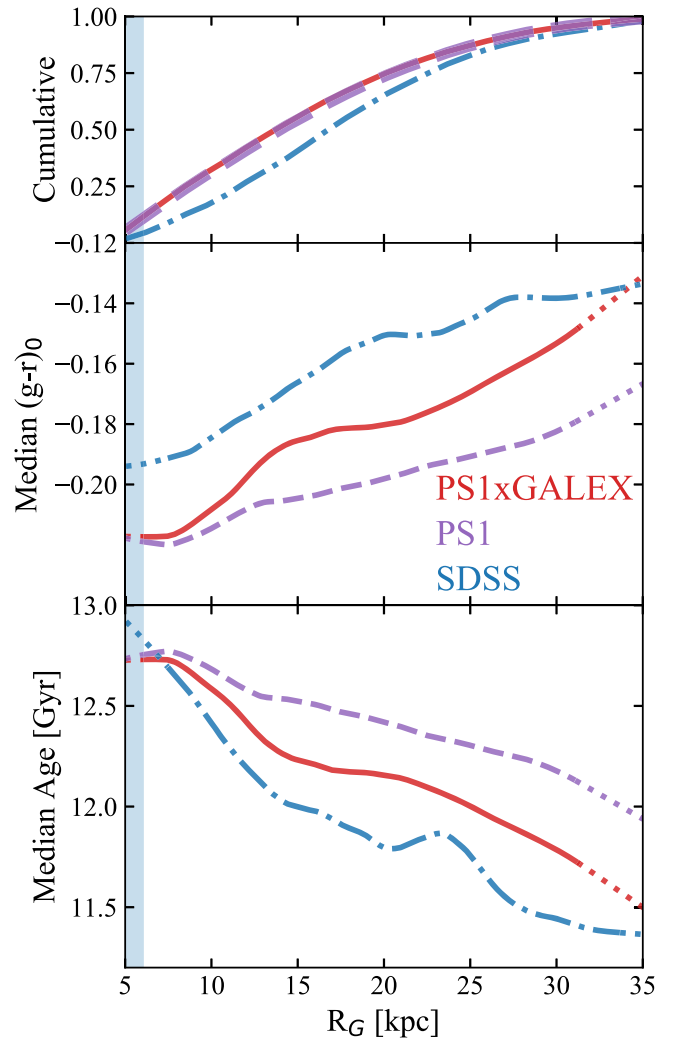


Figure 5. Top panel: cumulative distributions of the PS1xGALEX-SVC (red, solid), PS1- $(i-z)$ (violet, dashed), and SDSS spectroscopic (blue, dashed-dotted) samples, with respect to Galactocentric distance. Center panel: median $(g-r)_0$ color of the BHB samples as a function of Galactocentric distance. Bottom panel: median age of the BHB samples as a function of Galactocentric distance.

respectively. We again use LOWESS regression to visualize the profiles, with the local sampling fraction set to 25%. We mark the radial thresholds for each sample beyond which the star count drops below 5% of the sample, 29.7, 31, and 33.6 kpc for the PS1xGALEX-SVC, PS1- $(i-z)$, and SDSS spectroscopic catalogs, respectively.

We investigate the presence of a break radius in our BHB samples using MLE. We begin with a segmented linear model, defined as follows:

$$A(R_G) = A_0 + m_{\text{in}} \cdot R_G + (m_{\text{out}} - m_{\text{in}}) \cdot (R_G - R_b) \cdot H(R_G - R_b). \quad (6)$$

Here, A_0 is the intercept—the age at $R_G = 0$ —and m_{in} and m_{out} are the age gradients of the inner and outer linear profile, respectively, delineated by the break radius, R_b . We hereafter refer to the inner- and outer-halo regions, distinguished on the basis of the break radius, as the IHR and OHR, respectively. The Heaviside function, H , acts to switch from the IHR to OHR slope at the break radius. To build our likelihood function, we assume that the data are distributed about the segmented linear

model fit according to a Gaussian, for which we assign separate standard deviations, σ_{in} and σ_{out} , for the inner and outer profiles, respectively. The resulting probability function is

$$\rho(A_i | R_{G,i}; \theta) = \frac{1}{\sqrt{2\pi\sigma^2(R_{G,i})}} \exp\left[-\frac{(A_i - A(R_{G,i}|\theta))^2}{2\pi\sigma^2(R_{G,i})}\right]. \quad (7)$$

Here, $\sigma(R_G)$ is simply a step function:

$$\sigma(R_G) = \begin{cases} \sigma_{\text{in}}, & \text{if } R_G \leq R_b, \\ \sigma_{\text{out}}, & \text{if } R_G > R_b. \end{cases} \quad (8)$$

The model parameters, which we designate with θ , are then A_0 , m_{in} , m_{out} , R_b , σ_{in} , and σ_{out} . Our set of input parameters, \mathcal{X} , are simply the age, A_i , and Galactocentric radius, $R_{G,i}$. The optimal parameters are then determined using MLE. The corresponding log-likelihood function is

$$\begin{aligned} \ln \mathcal{L}(\theta | \mathcal{X}) &= \sum_i \ln \rho(\mathcal{X}_i | \theta) \\ &= -\sum_i \ln \sigma(R_{G,i}) - \frac{1}{2} \sum_i \left(\frac{A_i - A(R_{G,i}|\theta)}{\sigma(R_{G,i})} \right)^2. \end{aligned} \quad (9)$$

It is important that the segmented linear model in which a break radius is assumed be compared to a simple, no-break, linear model. In this case, the log-likelihood model is essentially identical, where we have substituted the segmented linear model of Equation (6) with a simple linear model. We discuss the goodness-of-fit comparisons in Section 5.

We determine best-fit parameters for our likelihood functions by sampling over the parameter space using the Python module `emcee` (Foreman-Mackey et al. 2013) implementation of Goodman & Weare's (2010) affine invariant Markov Chain Monte Carlo (MCMC) routine. For all samples, all model priors are taken to be uniform. We additionally assert that the intercept of our segmented and simple linear models, A_0 , not exceed 13.8 Gyr, and that the standard deviations, σ_{in} and σ_{out} , be positive. For the segmented linear model, we set the edges of the uniform prior to be at the minimum and maximum Galactocentric radii present in the sample. For the SDSS spectroscopic sample, however, we limit the break radius to $R_b < 22$ kpc, to avoid the otherwise uninteresting deviation seen to occur at ~ 23 kpc in the LOWESS age profile in Figure 5. While real, this deviation is likely an artifact of the small footprint of the SDSS spectroscopic sample, and thus is not representative of the underlying age profile.

4.5. Random Sample Consensus

Additionally, we estimate the slopes of the IHR and OHR profiles using a random sample consensus approach (RANSAC; Fischler & Bolles 1981). This nondeterministic algorithm achieves a consensus on the optimal linear model by iterative sampling of the data set, effectively mitigating outliers. First, we split the BHB samples by Galactocentric radius at an initial value of $R_b = 15.0$ kpc, and evaluate the gradient in each region separately. We then iterate the RANSAC linear parameter determination over 500 resamples of each region. In each iteration, we infer a break radius from the intersection of inner and outer age profiles. From these 500 estimates of m_{in} , m_{out} , and R_b , we determine the median value and standard deviation, the distributions of which are shown in Figure 6.

5. Results and Discussion

The parameters of the segmented linear model are determined for the Galactocentric radial age profiles of the three BHB catalogs described above, using MLE implemented with an MCMC routine. The resulting posterior distributions are shown for the PS1xGALEX-SVC sample in Figure 11, PS1-($i-z$) sample in Figure 12, and the SDSS spectroscopic sample in Figure 13. As a verification of the segmented linear model, we compare the maximized likelihood function with that of a simple linear model. To do so, we consider the Bayesian information criterion (BIC; Schwarz 1978). The BIC takes into account the goodness of fit for each model, while also penalizing the number of free parameters required by each, as a means of mitigating overfitting. This metric is defined as

$$\text{BIC} = -2 \ln \mathcal{L}_{\text{max}} + \text{dim}(\theta) \ln N, \quad (10)$$

where \mathcal{L}_{max} is the value of the likelihood function corresponding to the optimized parameters, θ , and N is the number of stars in the sample.

When comparing best-fit models, the preferred model is that which exhibits the lowest BIC value. We note that BIC values are only meaningful when compared against models in which the same samples are used. In other words, BIC values for one BHB sample may not be compared to another.

The BIC values for the linear, $\text{BIC}_{\text{linear}}$, and segmented linear, $\text{BIC}_{\text{break}}$, models were computed for each of the BHB samples, the results of which are listed in Table 1, where the bolded values indicated the smaller BIC. For each model, the difference between the linear and segmented model, ΔBIC , is in excess of 10^2 , where a $\Delta\text{BIC} > 10$ is considered very strong evidence against the model with the higher BIC. We conclude that, for all three BHB samples considered in this work, the segmented model is a significantly improved representation of the relative age distribution, as compared to a simple linear model.

As an independent verification of the segmented linear model, we performed RANSAC modeling on the inner- and outer-halo regions, inferring a break radius from the intersection of the linear profiles. The derived median age at $R_G = 0$ kpc, A_0 , the break radius, R_b , IHR age gradient, m_{in} , OHR age gradient, m_{out} , and their corresponding uncertainties for the RANSAC method and the maximum likelihood MCMC method are listed in Table 2.

The resulting IHR and OHR age gradients, as well as the break radius, vary significantly between the three BHB samples and indeed between the two methods included in this study. Particularly for the PS1xGALEX and PS1-($i-z$) sample, this variation is representative of the influence of the photometric selection function on the resulting radial age profile. The purity of the PS1-($i-z$) sample was estimated in Vickers et al. (2012) to be $\sim 74\%$, with a completeness of $\sim 57\%$, whereas we demonstrate using the SDSS spectroscopic sample a purity and completeness in excess of 80% for the PS1xGALEX-SVC sample. Both the PS1xGALEX-SVC sample and the SDSS spectroscopic sample exhibit a larger contrast in their IHR and OHR gradients than the PS1-($i-z$) sample. Further, as seen in Figure 5, and in both the MLE and RANSAC determinations in Table 2, the PS1xGALEX values are essentially intermediate to the PS1-($i-z$) and SDSS spectroscopic sample estimates. We therefore interpret this as an indication of our improved selection method, and conclude that the purity and completeness BHB samples are essential in order to reveal the contrasting signatures between the IHR and OHR.

For all three BHB samples, the IHR exhibits a significantly steeper age gradient than determined by previous studies that

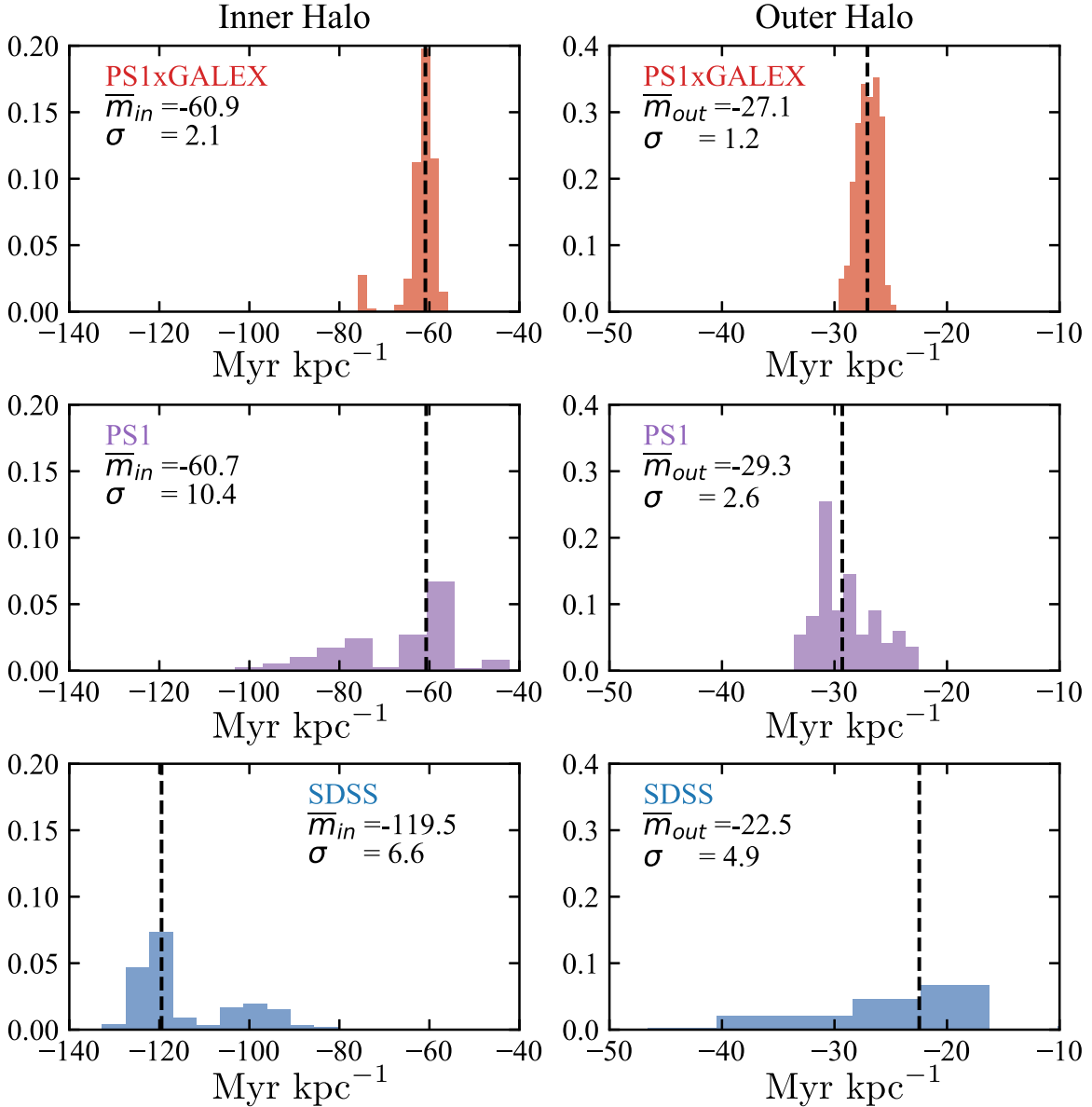


Figure 6. Distributions of Galactocentric radial age gradient estimates of the inner-halo (left panels) and outer-halo (right panels) regions. Gradients were determined for the PS1xGALEX (top), PS1- $(i-z)$ (middle), and SDSS spectroscopic (bottom) samples from 500 iterations of RANSAC regression, from which the mean \bar{m} and standard deviation σ estimates are shown and listed in Table 2.

Table 1
BIC for Age Models

BHB Sample Selection	BIC(linear)	BIC(break)	Δ BIC
PS1xGALEX-SVC	51,539	46,865	4674
PS1- $(i-z)$	63,295	60,245	3050
SDSS spectroscopic	8939	7978	961

treated the halo as a single profile: $-63.4 \pm 8.2 \text{ Myr kpc}^{-1}$, $-44.4 \pm 14.3 \text{ Myr kpc}^{-1}$, and $-84.3 \pm 14.6 \text{ Myr kpc}^{-1}$ for the PS1xGALEX-SVC, PS1- $(i-z)$, and SDSS spectroscopic samples, respectively. The gradient in the outer halo of $\sim -25 \text{ Myr kpc}^{-1}$, is consistent with previous studies (Carollo et al. 2016; Das et al. 2016). The three BHB samples studied in this work represent significantly different selection functions. The unanimity of the contrasting IHR and OHR age gradients, in addition to the superiority of the segmented linear regression model as compared

to a simple linear model, supports the conclusion that the break radius seen in the radial age profile is a true signature, as opposed to an artifact of the SVC selection function.

Both the age estimates corrected for metallicity and those inferred from $(g-r)_0$ color for the SDSS spectroscopic sample agree to within $\pm 130 \text{ Myr}$ within $10 < R_G < 27 \text{ kpc}$, thus the observed gradient in the relative age profile cannot be solely explained by a metallicity gradient in the Milky Way halo. Within $R_{GC} < 10$, Figure 4 the photometric age determination is seen to underestimate compared with the age estimates corrected for the spectroscopic metallicity. This suggests that, for the PS1xGALEX-SVC and PS1- $(i-z)$ samples, the IHR gradient is perhaps even steeper than determined in this study.

The difference in the median $(g-r)_0$ color between $5 < R_G(\text{kpc}) < 12$ of 0.018 mag for the PS1xGALEX-SVC sample corresponds to a difference in $(B-V)_0$ of $\sim 0.20 \text{ mag}$, roughly consistent with the Preston et al. (1991) result. Both

Table 2
Segmented Linear Profile Parameters for BHB Catalogs

BHB Sample Selection	A_0	σ_{A_0}	σ_{in}	σ_{out}	R_b	σ_{R_b}	m_{in}	$\sigma_{m_{\text{in}}}$	m_{out}	$\sigma_{m_{\text{out}}}$
	(Gyr)	(Gyr)	(Gyr)	(Gyr)	(kpc)	(kpc)	(Myr kpc ⁻¹)	(Myr kpc ⁻¹)	(Myr kpc ⁻¹)	(Myr kpc ⁻¹)
Maximum likelihood parameters										
PS1xGALEX-SVC	13.22	0.09	1.22	1.17	14.8	0.8	-63.4	8.2	-27.2	2.5
PS1-($i - z$)	13.12	0.13	1.04	1.07	11.0	1.3	-44.4	14.3	-21.3	1.6
SDSS spectroscopic	13.19	0.17	1.43	1.52	16.2	2.4	-84.3	14.6	-24.3	37.4
Random sample consensus parameters										
PS1xGALEX-SVC	13.2	0.02	1.21	1.18	14.7	0.6	-60.9	2.1	-27.1	1.2
PS1-($i - z$)	13.3	0.08	1.06	1.07	9.9	1.1	-60.7	7.4	-29.3	2.6
SDSS spectroscopic	13.6	0.05	1.45	1.48	13.2	0.6	-119.5	6.6	-22.5	4.9

the MLE and RANSAC results are roughly consistent with a break radius occurring at $R_G \sim 14$ kpc, although this value varies somewhat for each sample.

The scatter in the IHR and OHR age profiles, σ_{in} and σ_{out} , varies inversely with the sample size of the BHB selection; the largest scatter is seen in the SDSS spectroscopic sample ($N = 2695$), where $\sigma_{\text{out}} = 1.48$ Gyr, while the smallest is seen in the PS1-($i - z$) sample ($N = 20, 351$), where $\sigma_{\text{in}} = 1.04$ Gyr. We attribute the larger scatter seen for the SDSS spectroscopic sample to the smaller sample size and comparatively limited sky coverage. The resulting relative age profile is likely to be significantly more susceptible to deviations as a result of substructures in the halo, for instance the Virgo Overdensity (Vivas et al. 2001). It is reasonable to assume that, as larger samples of BHB stars are obtained from future large-sky surveys, the underlying radial age profile can be further constrained.

6. Interpretation

We compare our results to the Aquarius halo Aq-C-5 (Tissera et al. 2013), which best reproduced the outer-halo age profile in Carollo et al. (2018), for which our RANSAC method produces an IHR gradient of -30.0 ± 1.8 Myr kpc⁻¹. This value is somewhat smaller than our observational result of -63.4 ± 8.2 Myr kpc⁻¹, though a value of -48.6 ± 2.5 Myr kpc⁻¹ is obtained when considering only the accreted component of Aq-C-5. Considering that the median metallicity for the SDSS spectroscopic sample of $[\text{Fe}/\text{H}] = -1.75$ most closely resembles the median metallicity of the accreted component of Aq-C-5 (see Tissera et al. 2013, for details.), as opposed to the in situ component, it is possible that BHB stars selected in the manner outlined by this work are a natural probe of the halo’s accreted population. This is consistent with the result from Carollo et al. (2018), where the slope of the age profile is largely determined by the accreted stellar populations acquired in early stages of halo assembly. Complementary to these studies, Fernández-Alvar et al. (2019) showed that the more massive accreted satellites in Aq-C-5 (and Aq-D-5) have extended star formation activity, consistent with being gas-rich galaxies.

The contrasting age gradients between the inner and outer regions of the stellar halo may therefore reflect the contrasting roles of dissipational—i.e., gas-rich—and dissipationless mergers in the assembly histories of the halo components. In the dissipative merger scenario, star formation in gas-rich satellites can continue throughout the accretion event. Alternatively, where

dissipationless mergers occur, we expect a halo dominated by stars donated from smaller satellite galaxies with truncated star formation histories (Chiba & Beers 2000; Carollo et al. 2007, 2010). The break radius seen in the radial age profile could therefore represent the transition from an IHR dominated by dissipative mergers, to an OHR characterized by dissipationless accretion of lower mass sub-galactic fragments.

An open question is whether the ancient inner-halo structure proposed by Helmi et al. (2018) constitutes both the high-eccentricity component—the *Gaia* Sausage—previously identified by Belokurov et al. (2018), and the retrograde component of the halo, or if these structures represent distinct progenitor systems, as evidenced by Myeong et al. (2019). For an age gradient arising purely through accretion, according to the hierarchical process described in Amorisco (2017), our results favor two or more distinct progenitors of the inner halo. The proposed *Gaia*-Enceladus is thought to have undergone ~ 2 Gyr of star formation (Helmi et al. 2018). Considering the estimated infall time of ~ 10 Gyr ago, with the oldest members stars being 13 Gyr, *Gaia*-Enceladus likely was not forming stars by the infall time. Unless an extended star formation occurred in *Gaia*-Enceladus, or *Gaia*-Enceladus possessed a significant radial age gradient prior to accretion, the age gradient in BHB stars seems to rule out it being the single progenitor of the inner halo.

As suggested by Deason et al. (2018), the break radius seen in the stellar density profile at $R_G \sim 20$ kpc (Sesar et al. 2011) can be explained as the result of coincident apocentric radii of stars in the highly eccentric component of the halo. However, the break radius seen in the relative age profile of BHB stars occurs at a significantly smaller Galactocentric radius, $R_b \sim 14$ kpc. Considering the uncertainty in the stellar density break radius of ± 1 kpc (Xue et al. 2015), and the uncertainty in our determination of the break radius in the relative age profile of ± 2 kpc, we do not expect the break radius of the stellar density profile to be associated with the break radius in the relative age profile, and thus this discrepancy can be explained if at least two populations with characteristically distinct ages inhabit the region within the apocentric radius of the *Gaia* Sausage.

Alternatively, for an inner halo assembled from only a handful of relatively massive progenitor systems (Helmi et al. 2018; Myeong et al. 2018; Kruijssen et al. 2019; Lancaster et al. 2019), it is feasible that these systems retained sufficiently high gas-to-star ratios to enable persistent star formation

throughout the merger event. For an age gradient that is not instantiated by the accretion, and is thus driven by in situ star formation, we speculate that the steepness of the radial age profile might reflect the dynamics of the star formation history, mass-assembly rate, or gas contributions from the progenitor systems, provided that the number of progenitors is small. These gas-rich mergers would then be subject to ram pressure stripping during their interactions with the host halo (Simpson et al. 2018). While this pressure has the capability to remove cold gas from the satellite and quench star formation, the hot virialized gas in the host galaxy can act to shield the dwarf from both ram pressure stripping and UV-background heating. If we assume the infall of a few ($N \sim 3$) progenitors, as suggested from recent observational and simulation studies, then the spread in the BHB age distribution in the IHR of ~ 1.0 Gyr suggests either (1) a persistent star formation throughout the merger process, effectively constraining the thermal-to-ram pressure ratio (Hausammann et al. 2019) of the mergers that contributed to the formation of the inner halo, or (2) a significant contrast between the ages of the stellar populations contributed to the halo by the *Gaia* Sausage, Sequoia, and possibly additional dwarf systems yet to be identified.

7. Conclusions

Using selections of BHB stars from Pan-STARRS DR1 and *GALEX* photometry, we demonstrate the first evidence of a break radius in the relative age profile of the Milky Way, occurring at $R_{GC} \sim 14$ kpc. Within the break radius, we measure a significantly steeper age gradient than previous studies, -63.4 ± 8.2 Myr kpc^{-1} . A novel methodology was developed for the selection of BHB stars from photometry, using 3D support vector classification. We demonstrate, using the catalog of spectroscopically confirmed BHBs from Santucci et al. (2015a), that we have achieved an unprecedented selection purity, $\sim 80\%$. Age distributions inferred from photometry are offset slightly from those determined from BHB population synthesis, which corrects for influence of metallicity, but otherwise preserve the gradient signature, verifying the use of photometric colors as a reasonable approximation of relative age for BHB samples.

Our results confirm that $(g - r)_0$ gradient in BHB stars corresponds to a negative age gradient consistent with the “inside-out” formation model, wherein the oldest halo stars populate the inner-halo region. The contrasting age gradients in the inner- and outer-halo region suggest that the inner and outer haloes have fundamentally different formation histories. We postulate that the steeper age gradient seen in the inner-halo region is evidence of the dissipational formation of the inner halo, consisting of a few massive progenitor systems. The existence of a break radius and unique age gradients in the inner- and outer-halo regions provide additional constraints for simulations of galactic formation, particularly for the inferred mass-assembly and merger-tree histories of the Milky Way.

The authors thank the referee for their comments, which substantially improved our analysis. D.D.W., T.C.B., V.M.P., and P.D. acknowledge partial support for this work from grant PHY 14-30152; Physics Frontier Center/JINA Center for the Evolution of the Elements (JINA-CEE), awarded by the US National Science Foundation. T.C.B. acknowledges partial support from the Leverhulme Trust (UK), which hosted his visiting professorship at the University of Hull during the completion of this study.

R.M.S. gratefully acknowledges Conselho Nacional de Desenvolvimento Científico e Tecnológico (CNPq, process No 436696/2018-5).

The Pan-STARRS1 Surveys (PS1) and the PS1 public science archive have been made possible through contributions by the Institute for Astronomy, the University of Hawaii, the Pan-STARRS Project Office, the Max Planck Society and its participating institutes, the Max Planck Institute for Astronomy, Heidelberg and the Max Planck Institute for Extraterrestrial Physics, Garching, The Johns Hopkins University, Durham University, the University of Edinburgh, the Queen’s University Belfast, the Harvard-Smithsonian Center for Astrophysics, the Las Cumbres Observatory Global Telescope Network Incorporated, the National Central University of Taiwan, the Space Telescope Science Institute, the National Aeronautics and Space Administration under grant No. NNX08AR22G issued through the Planetary Science Division of the NASA Science Mission Directorate, the National Science Foundation grant No. AST-1238877, the University of Maryland, Eotvos Lorand University (ELTE), the Los Alamos National Laboratory, and the Gordon and Betty Moore Foundation.

Funding for the Sloan Digital Sky Survey IV has been provided by the Alfred P. Sloan Foundation, the U.S. Department of Energy Office of Science, and the Participating Institutions. SDSS-IV acknowledges support and resources from the Center for High-Performance Computing at the University of Utah. The SDSS website is www.sdss.org. SDSS-IV is managed by the Astrophysical Research Consortium for the Participating Institutions of the SDSS Collaboration, including the Brazilian Participation Group, the Carnegie Institution for Science, Carnegie Mellon University, the Chilean Participation Group, the French Participation Group, Harvard-Smithsonian Center for Astrophysics, Instituto de Astrofísica de Canarias, The Johns Hopkins University, Kavli Institute for the Physics and Mathematics of the Universe (IPMU)/University of Tokyo, the Korean Participation Group, Lawrence Berkeley National Laboratory, Leibniz Institut für Astrophysik Potsdam (AIP), Max Planck Institut für Astronomie (MPIA Heidelberg), Max Planck Institut für Astrophysik (MPA Garching), Max Planck Institut für Extraterrestrische Physik (MPE), National Astronomical Observatories of China, New Mexico State University, New York University, University of Notre Dame, Observatório Nacional/MCTI, The Ohio State University, Pennsylvania State University, Shanghai Astronomical Observatory, United Kingdom Participation Group, Universidad Nacional Autónoma de México, University of Arizona, University of Colorado Boulder, University of Oxford, University of Portsmouth, University of Utah, University of Virginia, University of Washington, University of Wisconsin, Vanderbilt University, and Yale University.

Appendix

In this section, we present the relative age projections in Galactocentric X versus Z (Figure 7), Y versus Z (Figure 8), and X versus Y (Figure 9) coordinates, for each of the BHB samples described in the text. We provide the X versus Z age distributions of the SDSS spectroscopic sample from Santucci et al. (2015a) in Figure 10, for both photometric estimates and corrected estimates from Denissenkov et al. (2017). We present the resulting posterior probability distributions from the MLE for each the PS1xGALEX-SVC sample (Figure 11), the PS1- $(i - z)$ sample (Figure 12), and the SDSS spectroscopic sample (Figure 13).

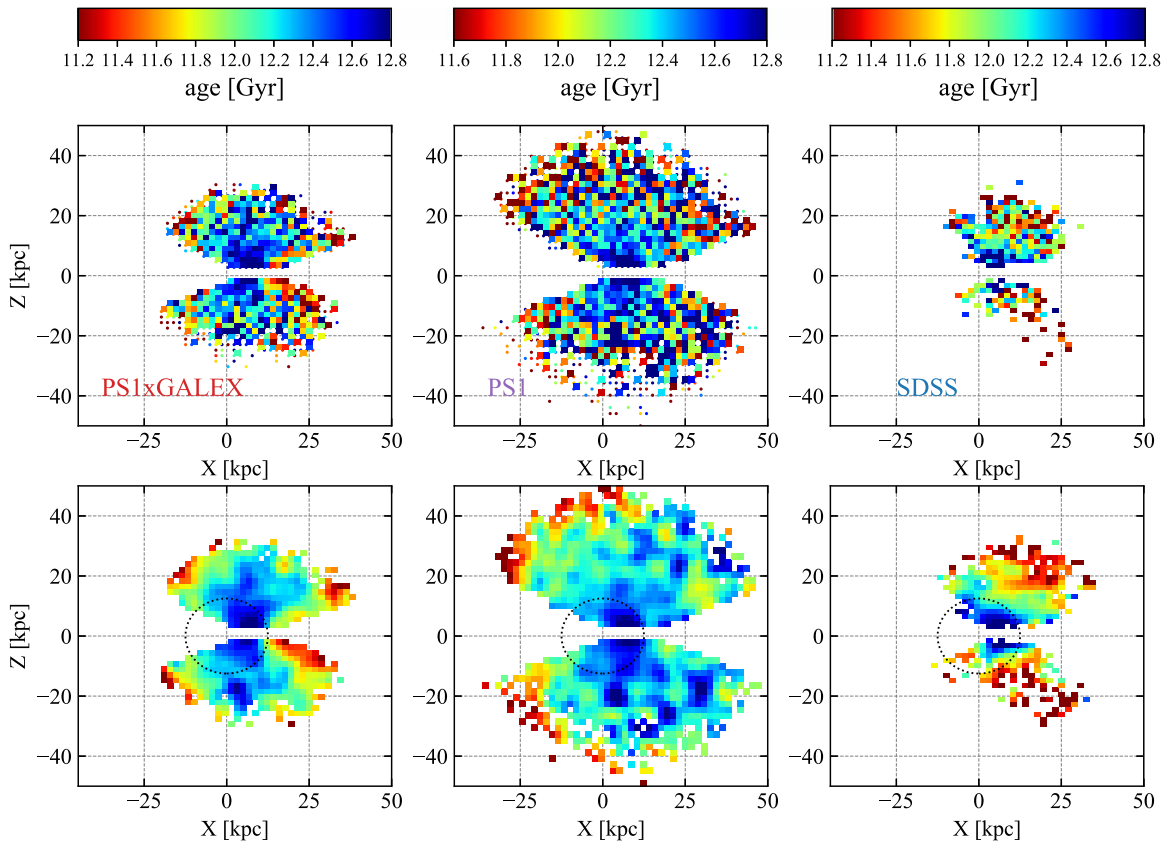


Figure 7. Projections of Galactocentric X vs. Z for the PS1xGALEX (left), PS1- $(i - z)$ (center), and SDSS spectroscopic (right) samples. The dotted circle represents the approximate transition from the IHR to the OHR, $R_G = 12.5$ kpc.

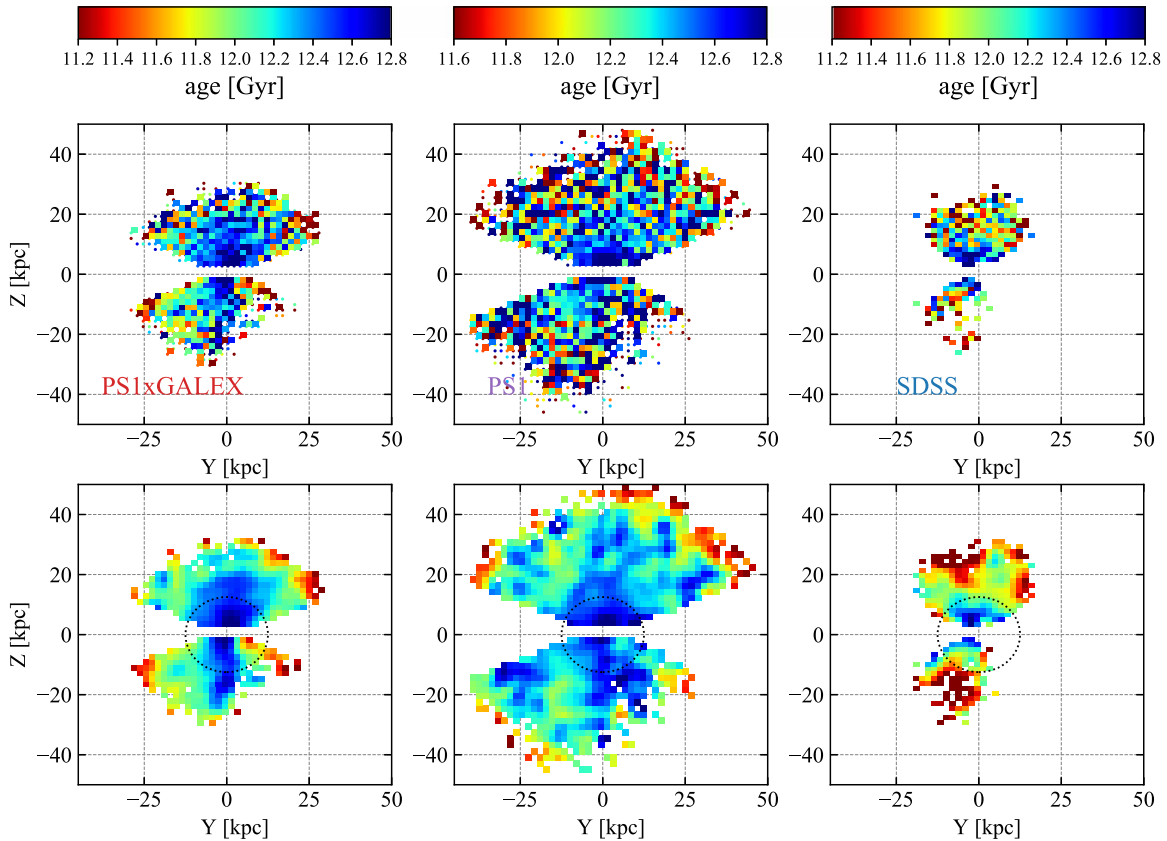


Figure 8. Projections of Galactocentric Y versus Z for the PS1xGALEX (left), PS1- $(i - z)$ (center), and SDSS spectroscopic (right) samples. The dotted circle represents the approximate transition from the IHR to the OHR, $R_G = 12.5$ kpc.

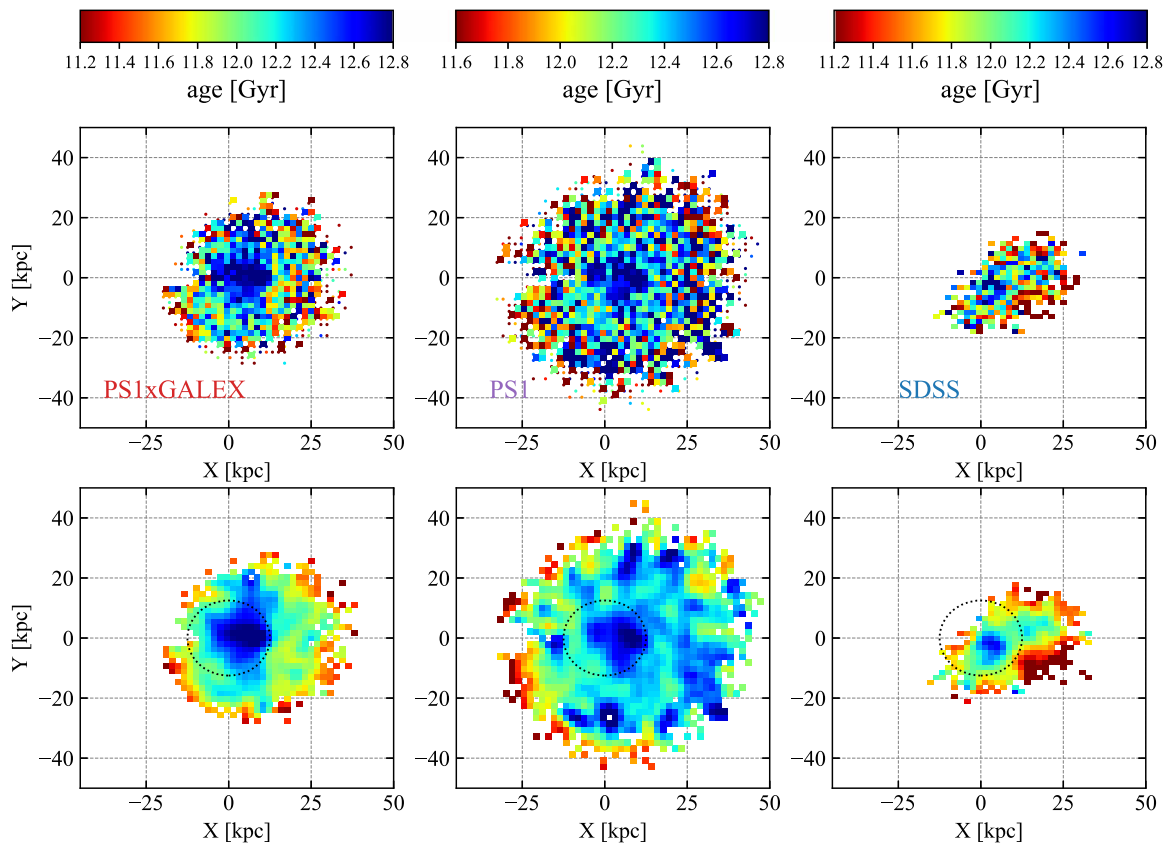


Figure 9. Projections of Galactocentric X versus Y for the PS1xGALEX (*left*), PS1- $(i - z)$ (*center*), and SDSS spectroscopic (*right*) samples. The dotted circle represents the approximate transition from the IHR to the OHR, $R_G = 12.5$ kpc.

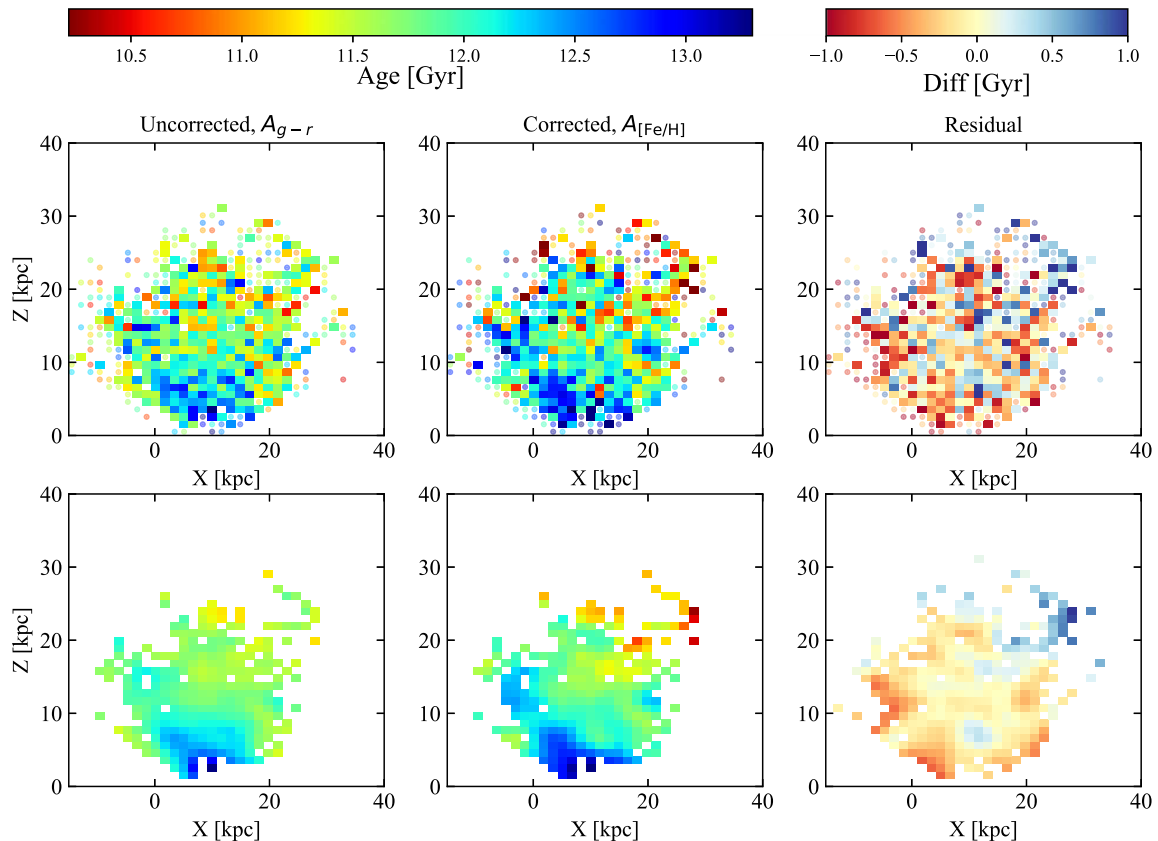


Figure 10. Age distributions of the SDSS spectroscopic sample from Santucci et al. (2015a), for both photometric estimates and corrected estimates from Denissenkov et al. (2017).

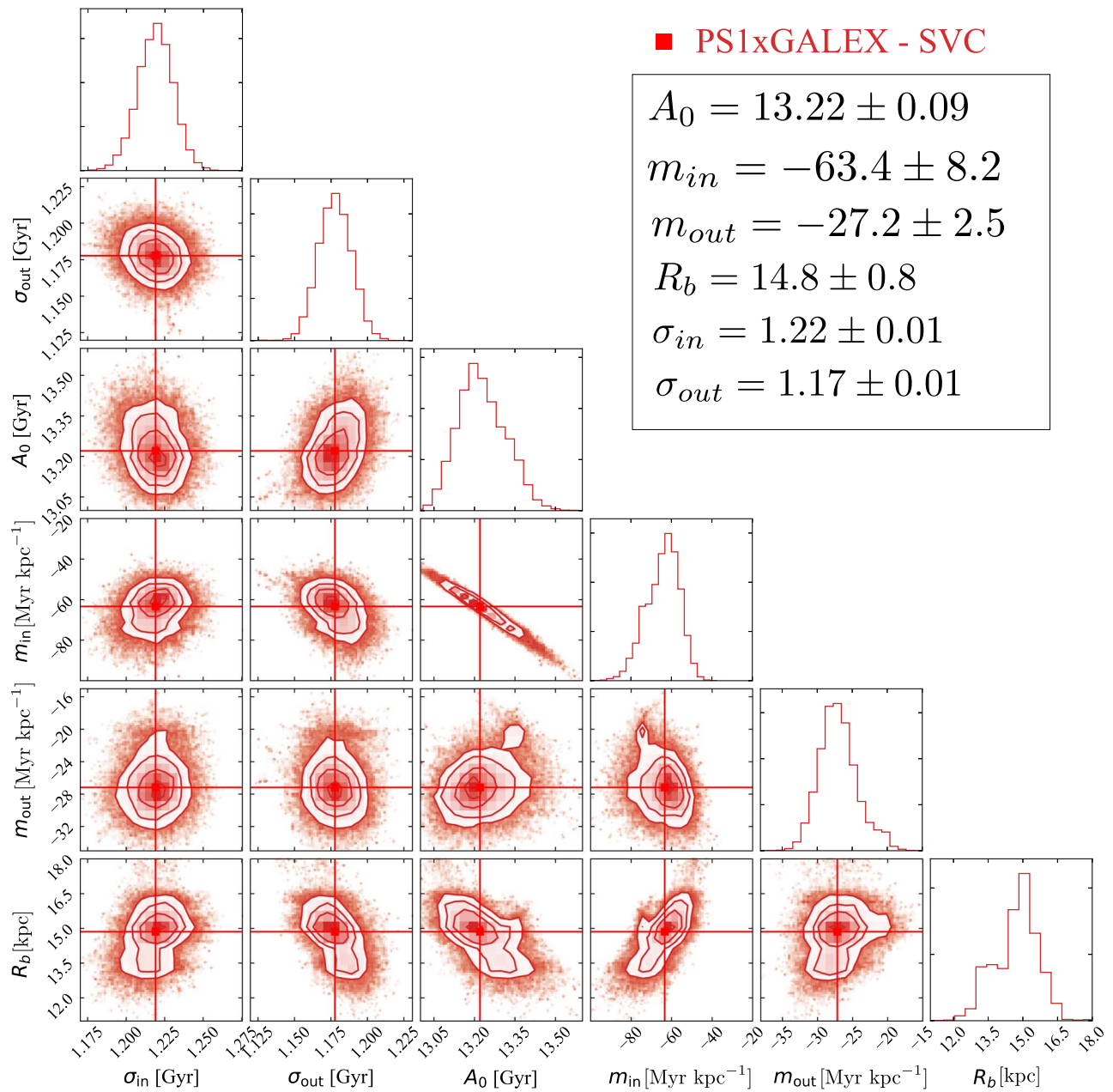


Figure 11. Posterior probability distributions of parameters (σ_{in} , σ_{out} , A_0 , m_{in} , m_{out} , R_b) of the segmented linear regression model for the PS1xGALEX-SVC sample. The red lines and squares correspond to the most likely values.

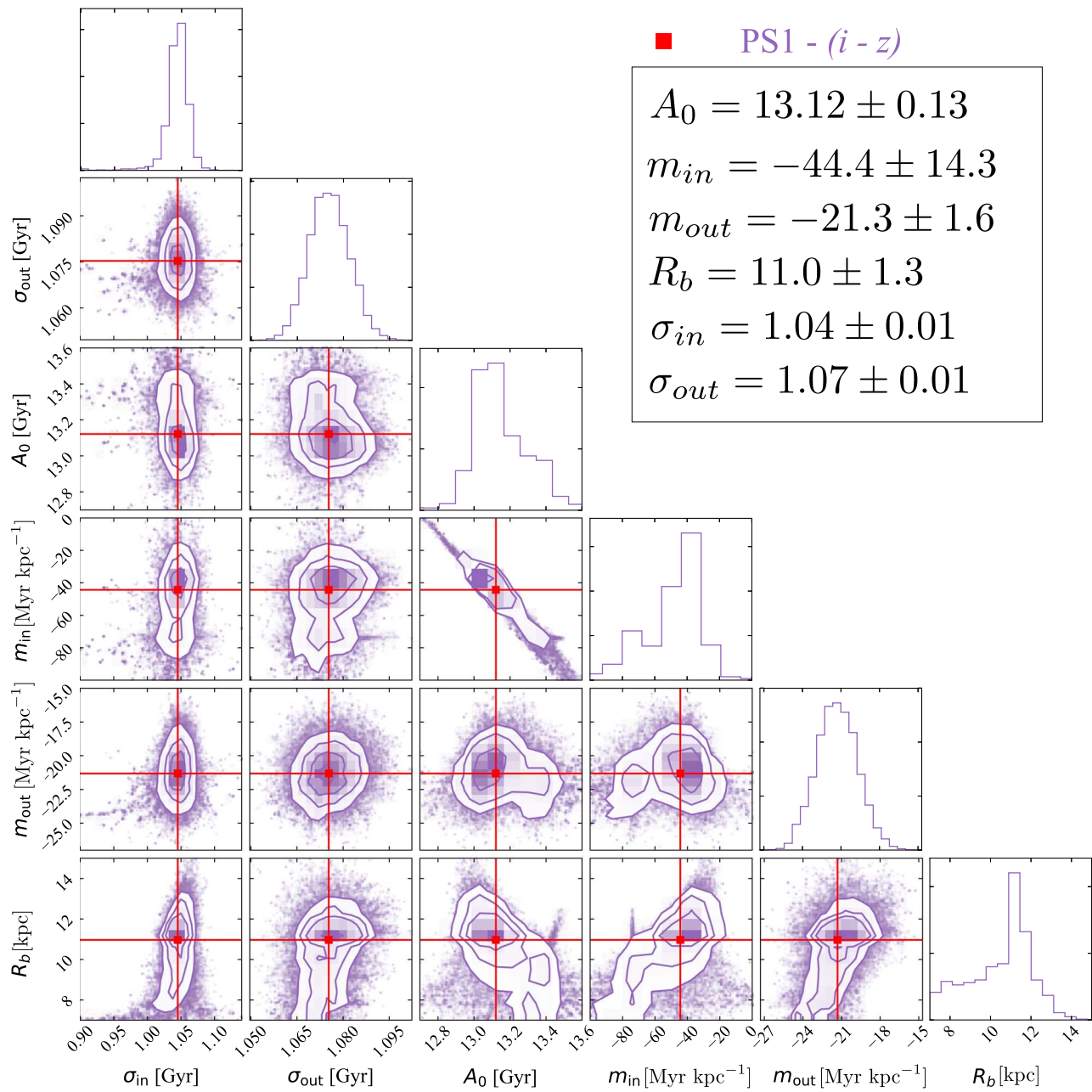


Figure 12. Posterior probability distributions of parameters (σ_{in} , σ_{out} , A_0 , m_{in} , m_{out} , R_b) of the segmented linear regression model for the PS1-(*i* - *z*) sample. The red lines and squares correspond to the most likely values.

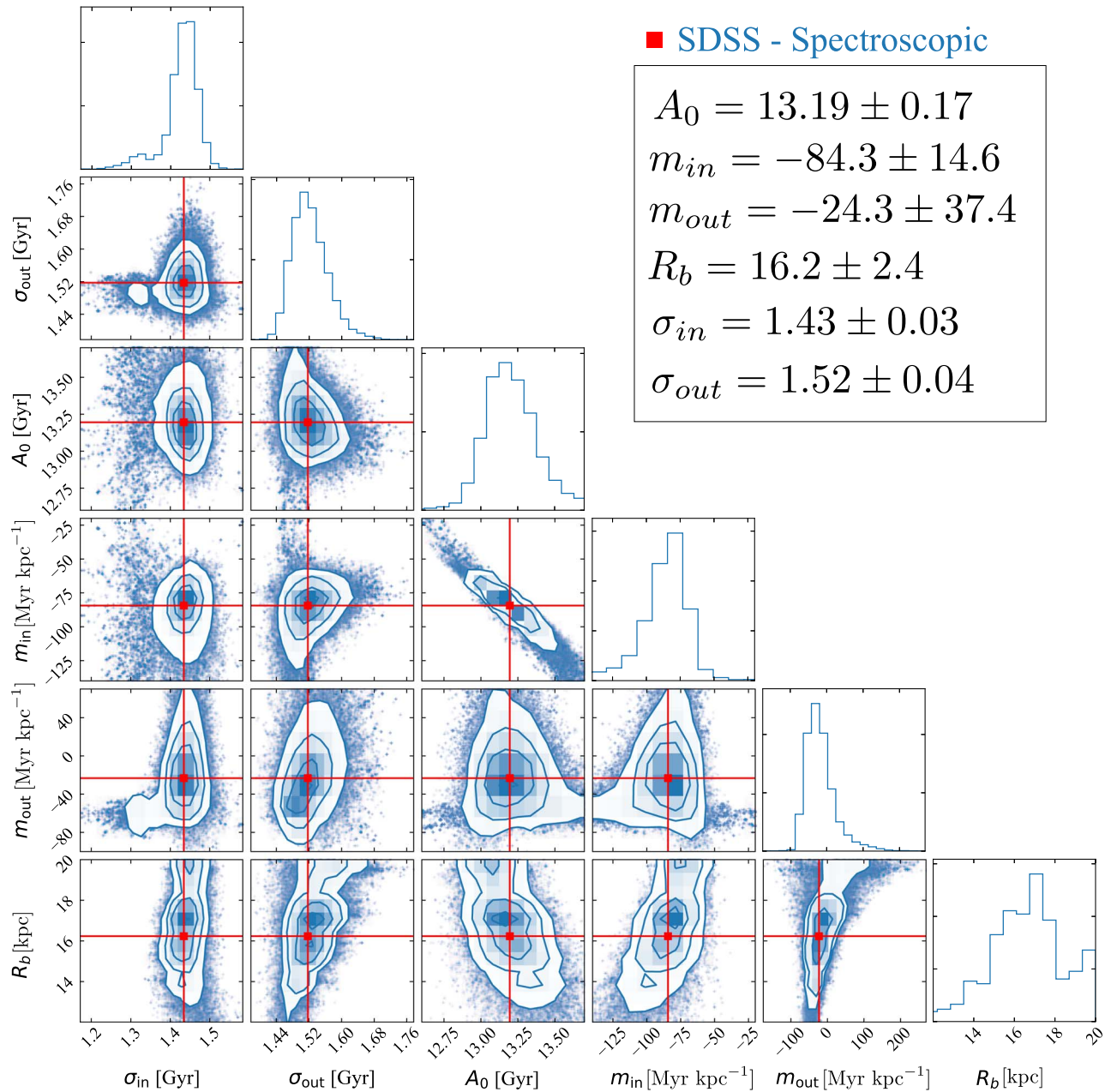


Figure 13. Posterior probability distributions of parameters (σ_{in} , σ_{out} , A_0 , m_{in} , m_{out} , R_b) of the segmented linear regression model for the SDSS spectroscopic sample. The red lines and squares correspond to the most likely values.

ORCID iDs

Devin D. Whitten <https://orcid.org/0000-0002-9594-6143>
 Timothy C. Beers <https://orcid.org/0000-0003-4573-6233>
 Vinicius M. Placco <https://orcid.org/0000-0003-4479-1265>
 Rafael M. Santucci <https://orcid.org/0000-0002-7529-1442>
 Pavel Denissenkov <https://orcid.org/0000-0001-6120-3264>
 Patricia B. Tissera <https://orcid.org/0000-0001-5242-2844>
 Nina Hernitschek <https://orcid.org/0000-0003-1681-0430>
 Daniela Carollo <https://orcid.org/0000-0003-4710-132X>

References

Abazajian, K. N., Adelman-McCarthy, J. K., Agüeros, M. A., et al. 2009, *ApJS*, **182**, 543
 Abolfathi, B., Aguado, D. S., Aguilar, G., et al. 2018, *ApJS*, **235**, 42
 Aihara, H., Allende Prieto, C., An, D., et al. 2011a, *ApJS*, **195**, 26

Aihara, H., Allende Prieto, C., An, D., et al. 2011b, *ApJS*, **193**, 29
 Allende Prieto, C., Sivarani, T., Beers, T. C., et al. 2008, *AJ*, **136**, 2070
 Amorisco, N. C. 2017, *MNRAS*, **464**, 2882
 Asplund, M., Grevesse, N., Sauval, A. J., & Scott, P. 2009, *ARA&A*, **47**, 481
 Barbá, R. H., Minniti, D., Geisler, D., et al. 2019, *ApJL*, **870**, L24
 Beers, T. C., Carollo, D., Ivezić, Ž., et al. 2012, *ApJ*, **746**, 34
 Beers, T. C., & Christlieb, N. 2005, *ARA&A*, **43**, 531
 Belokurov, V., Erkal, D., Evans, N. W., Koposov, S. E., & Deason, A. J. 2018, *MNRAS*, **478**, 611
 Belokurov, V., Zucker, D. B., Evans, N. W., et al. 2006, *ApJL*, **642**, L137
 Bensby, T., Yee, J. C., Feltzing, S., et al. 2013, *A&A*, **549**, A147
 Bianchi, L., Shiao, B., & Thilker, D. 2017, *ApJS*, **230**, 24
 Carollo, D., Beers, T. C., Chiba, M., et al. 2010, *ApJ*, **712**, 692
 Carollo, D., Beers, T. C., Lee, Y. S., et al. 2007, *Natur*, **450**, 1020
 Carollo, D., Beers, T. C., Placco, V. M., et al. 2016, *NatPh*, **12**, 1170
 Carollo, D., Tissera, P. B., Beers, T. C., et al. 2018, *ApJL*, **859**, L7
 Chambers, K. C., Magnier, E. A., Metcalfe, N., et al. 2016, arXiv:1612.05560 [astro-ph.IM]
 Chiba, M., & Beers, T. C. 2000, *AJ*, **119**, 2843

- Cleveland, W. S. 1979, *J. Am. Stat. Assoc.*, 74, 829
- Das, P., Williams, A., & Binney, J. 2016, *MNRAS*, 463, 3169
- Dawson, K. S., Schlegel, D. J., Ahn, C. P., et al. 2013, *AJ*, 145, 10
- Deason, A. J., Belokurov, V., & Evans, N. W. 2011, *MNRAS*, 416, 2903
- Deason, A. J., Belokurov, V., Koposov, S. E., & Lancaster, L. 2018, *ApJL*, 862, L1
- de Jong, J. T. A., Yanny, B., Rix, H.-W., et al. 2010, *ApJ*, 714, 663
- Denissenkov, P. A., VandenBerg, D. A., Kopacki, G., & Ferguson, J. W. 2017, *ApJ*, 849, 159
- Farrow, D. J., Cole, S., Metcalfe, N., et al. 2014, *MNRAS*, 437, 748
- Fattahi, A., Belokurov, V., Deason, A. J., et al. 2019, *MNRAS*, 484, 4471
- Fernández-Alvar, E., Tissera, P. B., Carigi, L., et al. 2019, *MNRAS*, 485, 1745
- Fischler, M. A., & Bolles, R. C. 1981, *Commun. ACM*, 24, 381
- Flewelling, H. A., Magnier, E. A., Chambers, K. C., et al. 2016, arXiv:1612.05243 [astro-ph.IM]
- Font, A. S., McCarthy, I. G., Crain, R. A., et al. 2011, *MNRAS*, 416, 2802
- Foreman-Mackey, D., Hogg, D. W., Lang, D., & Goodman, J. 2013, *PASP*, 125, 306
- Freeman, K., & Bland-Hawthorn, J. 2002, *ARA&A*, 40, 487
- Fukushima, T., Chiba, M., Homma, D., et al. 2018, *PASJ*, 70, 69
- Gaia Collaboration, Brown, A. G. A., Vallenari, A., et al. 2018, *A&A*, 616, A1
- Gattano, C., Andrei, A. H., Coelho, B., et al. 2018, *A&A*, 614, A140
- Goodman, J., & Weare, J. 2010, *CAMCS*, 5, 65
- Grady, J., Belokurov, V., & Evans, N. W. 2019, *MNRAS*, 483, 3022
- Gratton, R. G., Carretta, E., Desidera, S., et al. 2003, *A&A*, 406, 131
- Hausammann, L., Revaz, Y., & Jablonka, P. 2019, *A&A*, 624, A11
- Helmi, A. 2008, *A&ARv*, 15, 145
- Helmi, A., Babusiaux, C., Koppelman, H. H., et al. 2018, *Natur*, 563, 85
- Hernitschek, N., Cohen, J. G., Rix, H.-W., et al. 2018, *ApJ*, 859, 31
- Jolliffe, I. T. 2002, *Principal Component Analysis* (Berlin: Springer)
- Kheirdastan, S., & Bazarghan, M. 2016, *Ap&SS*, 361, 304
- Koppelman, H., Helmi, A., & Veljanoski, J. 2018, *ApJL*, 860, L11
- Kruijssen, J. M. D., Pfeffer, J. L., Reina-Campos, M., Crain, R. A., & Bastian, N. 2019, *MNRAS*, 486, 3180
- Lancaster, L., Koposov, S. E., Belokurov, V., Evans, N. W., & Deason, A. J. 2019, *MNRAS*, 486, 378
- Law, D. R., Majewski, S. R., & Johnston, K. V. 2009, *ApJL*, 703, L67
- Leaman, R., VandenBerg, D. A., & Mendel, J. T. 2013, *MNRAS*, 436, 122
- Lee, Y. S., Beers, T. C., Sivarani, T., et al. 2008a, *AJ*, 136, 2022
- Lee, Y. S., Beers, T. C., Sivarani, T., et al. 2008b, *AJ*, 136, 2050
- Majewski, S. R., Skrutskie, M. F., Weinberg, M. D., & Ostheimer, J. C. 2003, *ApJ*, 599, 1082
- Marrese, P. M., Marinoni, S., Fabrizio, M., & Altavilla, G. 2019, *A&A*, 621, A144
- Martig, M., Minchev, I., Ness, M., Fouesneau, M., & Rix, H.-W. 2016, *ApJ*, 831, 139
- Martin, D. C., Fanson, J., Schiminovich, D., et al. 2005, *ApJL*, 619, L1
- Martin, N. F., Ibata, R. A., Rich, R. M., et al. 2014, *ApJ*, 787, 19
- Mateu, C., & Vivas, A. K. 2018, *MNRAS*, 479, 211
- Miceli, A., Rest, A., Stubbs, C. W., et al. 2008, *ApJ*, 678, 865
- Minchev, I., Martig, M., Streich, D., et al. 2015, *ApJL*, 804, L9
- Myeong, G. C., Evans, N. W., Belokurov, V., Sanders, J. L., & Koposov, S. E. 2018, *ApJL*, 863, L28
- Myeong, G. C., Vasiliev, E., Iorio, G., Evans, N. W., & Belokurov, V. 2019, *MNRAS*, 488, 1235
- Nelson, D., Pillepich, A., Genel, S., et al. 2015, *A&C*, 13, 12
- Nissen, P. E., & Schuster, W. J. 2010, *A&A*, 511, L10
- Paxton, B., Bildsten, L., Dotter, A., et al. 2011, *ApJS*, 192, 3
- Paxton, B., Cantiello, M., Arras, P., et al. 2013, *ApJS*, 208, 4
- Pedregosa, F., Varoquaux, G., Gramfort, A., et al. 2011, *J. Mach. Learn. Res.*, 12, 2825
- Pei, Y. C. 1995, *ApJ*, 438, 623
- Pillepich, A., Vogelsberger, M., Deason, A., et al. 2014, *MNRAS*, 444, 237
- Placco, V. M., Frebel, A., Lee, Y. S., et al. 2015, *ApJ*, 809, 136
- Preston, G. W., Shectman, S. A., & Beers, T. C. 1991, *ApJ*, 375, 121
- Raftery, A. E. 1995, *Sociological Methodology*, 25, 111
- Saha, A. 1985, *ApJ*, 289, 310
- Santucci, R. M., Beers, T. C., Placco, V. M., et al. 2015a, *ApJL*, 813, L16
- Santucci, R. M., Placco, V. M., Rossi, S., et al. 2015b, *ApJ*, 801, 116
- Schlaflly, E. F., & Finkbeiner, D. P. 2011, *ApJ*, 737, 103
- Schlegel, D. J., Finkbeiner, D. P., & Davis, M. 1998, *ApJ*, 500, 525
- Schwarz, G. 1978, *AnSta*, 6, 461
- Sesar, B., Jurić, M., & Ivezić, Ž. 2011, *ApJ*, 731, 4
- Shipp, N., Drlica-Wagner, A., Balbinot, E., et al. 2018, *ApJ*, 862, 114
- Simpson, C. M., Grand, R. J. J., Gómez, F. A., et al. 2018, *MNRAS*, 478, 548
- Sirko, E., Goodman, J., Knapp, G. R., et al. 2004, *AJ*, 127, 899
- Sluis, A. P. N., & Arnold, R. A. 1998, *MNRAS*, 297, 732
- Springel, V., Wang, J., Vogelsberger, M., et al. 2008, *MNRAS*, 391, 1685
- Thomas, G. F., McConnachie, A. W., Ibata, R. A., et al. 2018, *MNRAS*, 481, 5223
- Tissera, P. B., Beers, T. C., Carollo, D., & Scannapieco, C. 2014, *MNRAS*, 439, 3128
- Tissera, P. B., Scannapieco, C., Beers, T. C., & Carollo, D. 2013, *MNRAS*, 432, 3391
- Tissera, P. B., White, S. D. M., & Scannapieco, C. 2012, *MNRAS*, 420, 255
- Tonry, J. L., Stubbs, C. W., Lykke, K. R., et al. 2012, *ApJ*, 750, 99
- Vickers, J. J., Grebel, E. K., & Huxor, A. P. 2012, *AJ*, 143, 86
- Vickers, J. J., Huxor, A. P., & Grebel, E. K. 2014, *EAS Publications Series*, 67, 183
- Vivas, A. K., Zinn, R., Andrews, P., et al. 2001, *ApJL*, 554, L33
- Wang, H., López-Corredoira, M., Carlin, J. L., & Deng, L. 2018, *MNRAS*, 477, 2858
- White, S. D. M., & Rees, M. J. 1978, *MNRAS*, 183, 341
- Xue, X.-X., Rix, H.-W., Ma, Z., et al. 2015, *ApJ*, 809, 144
- Xue, X. X., Rix, H. W., Zhao, G., et al. 2008, *ApJ*, 684, 1143
- Yanny, B., Newberg, H. J., Kent, S., et al. 2000, *ApJ*, 540, 825
- Yanny, B., Rockosi, C., Newberg, H. J., et al. 2009, *AJ*, 137, 4377
- Zolotov, A., Willman, B., Brooks, A. M., et al. 2009, *ApJ*, 702, 1058